Peer-reviewed version available at *Materials* **2018**, *11*, 2018; doi:10.3390/ma11102018

Article

Incipient Bulk Polycrystal Plasticity Observed by Synchrotron in-situ Topotomography

Henry Proudhon [1,*], Nicolas Guéninchault [1,†], Samuel Forest [1] and Wolfgang Ludwig [2,3]

1 MINES ParisTech, PSL Research University, MAT - Centre des matériaux, CNRS UMR 7633, BP 87 91003 Evry, France; samuel.forest@mines-paristech.fr; henry.proudhon@mines-paristech.fr
2 ESRF, The European Synchrotron, CS 40220, 38043 Grenoble, France; ludwig@esrf.fr
3 University of Lyon, INSA Lyon, MATEIS, UMR 5510 CNRS, F-69621 LYON, France
* Correspondence: henry.proudhon@mines-paristech.fr; Tel.: +33-160-763-070
† Current address: Xnovo Technology ApS, Theilgaards Alle 9, 1th, 4600 Køge, Denmark

Abstract: In this paper, we present a comprehensive 4D study of the early stage of plastic deformation in a polycrystalline binary AlLi alloy. The entire microstructure is mapped with X-ray diffraction contrast tomography and a set of bulk grains is further studied via X-ray topotomography during mechanical loading. The observed contrast is analyzed with respect to the slip system activation and the evolution of the orientation spread is measured as a function of applied strain. The experimental observations are augmented by the mechanical response predicted by crystal plasticity finite element simulations to analyze the onset of plasticity in details. Simulation results show a general agreement of the individual slip system activation during loading and that comparison with experiments at the length scale of the grains may be used to fine tune the constitutive model parameters.

Keywords: Polycrystal plasticity; X-ray diffraction imaging; Topotomography; in situ experiment; Finite element simulation, lattice curvature, rocking curve.

1. Introduction

Determining microstructure-property relationships is an essential engineering problem and is directly linked to our ability to observe both the microstructure and the deformation/failure mechanisms concurrently. Electron back scattered diffraction (EBSD) which provides crystal orientation maps with sub-micrometer spatial resolution remains a key tool but is limited to the specimen surface [1]. To measure and interpret the strain field produced within individual grains, digital image correlation can be used provided a small-enough speckle can be produce at the specimen surface [2,3]. In this regard, subsequent analysis using numerical methods such as finite elements has also proved to be a powerful tool to interpret experimental results [4–6], but ultimately remains limited if the underlying material volume is not known [7]. In this paper, a new method combining in situ mechanical testing, three dimensional (3D) bulk X-ray inspections and crystal plasticity finite elements method (CPFEM) is used to study how plasticity proceeds in individual grains of a polycrystalline sample.

In the last 10 years, one particular focus of the 3D imaging community has been on obtaining reliable three-dimensional grain maps. Since most structural materials are polycrystalline and the mechanical properties are determined by their internal microstructure, this is a critical issue. For instance, considering slip transmission in crystal plasticity problems or small tortuous cracks evolving in a 3D grain network, it is a recurring challenge to assess the bulk mechanisms from surface observations only. Knowing how the different grains of the microstructure are arranged below the surface is therefore essential. Therefore, there has been considerable effort to develop characterization techniques at the meso-scale, which can image typically 1 mm^3 of material with a spatial resolution in the order of the micrometer.

Among 3D characterization, an important distinction exists between destructive and non-destructive techniques. Serial sectioning relies on repeated 2D imaging (which may include several modalities) of individual slices where a thin layer of material is removed between each observation [8]. Considerable progress on that side has been made in the last decade, bringing high quality measurements in 3D of grain sizes and orientations, but also detailed grain shapes and grain boundary characters. The price to pay with serial sectioning remains, however, the destruction of the sample. In parallel, accessing crystallographic information in the bulk of polycrystalline specimens was subsequently achieved by using the high penetration power of hard X-rays and leveraging diffraction contrast. This led to the development of a variety of 3D X-ray diffraction techniques (3DXRD, see [9] and [10]) enabling the the characterization of millimetre sized specimens by tracking the diffraction of each individual crystal within the material volume while rotating the specimen. Among them, the near field variant called X-ray Diffraction Contrast Tomography (DCT) uses an extended box beam to illuminate the specimen and allows for simultaneous reconstruction of both, the sample microstructure visible in X-ray absorption contrast and the crystallographic grain microstructure as determined from the diffraction signals with a single tomographic scan provided the grains have a limited orientation spread [11–13]. The typical acquisition time is one hour on a high brilliance beam line such as ID11 at ESRF, which makes it the fastest non-destructive grain mapping technique.

Non destructive imaging allows to observe both the microstructure and the deformation/failure mechanisms in situ (4D studies). But resolving 3D grain shapes by near-field diffraction imaging requires to reduce the sample to detector distance to a few millimeters, which has for a long time drastically limited mechanical 4D studies due to the space constraints. Recent progresses with mechanical stress rigs solved this issue and opened new perspectives to study the deformation and fracture of polycrystalline materials [14,15].

Another key challenge is to link 3D microstructure characterization tools with computational models in order to predict engineering mechanical properties. This can be done using synthetically generated images, but it requires using sophisticated models to ensure the microstructure is representative, in particular of the tail distributions (critical when looking at fracture processes) [16]. Another approach is to use as-measured 3D microstructures [17]. The major advantage of this route is to directly compare experiment and mechanical simulation at the grain scale. For mechanical problems, continuum crystal plasticity (either using the finite elements or the spectral method to solve the equilibrium) has proved to be a powerful tool to interpret experimental results obtained in the deformation of metallic polycrystals [4,18–20]. Large scale 3D polycrystalline simulations can be performed with sufficient local discretization to predict the transgranular plastic strain fields. One of the issue of this type of models is the material parameters identification. This is mostly due to the fact that identification is classically done by minimizing a cost function versus macroscopic tests response which makes the problem ill posed. Some recent attempts directly used local strain measurements in the identification data set in order to identify material model parameters [21] but have remained limited to surface studies so far.

In this paper, we present a new 4D study, using a combination of X-ray diffraction contrast tomography, topotomography and phase contrast tomography to study polycrystal plasticity. Experimental and simulation methods are detailed in section 2. The main experimental results are then presented in sections 3.1 for the observed slip system activation and 3.2 for the measured crystal lattice orientation. Simulation results and comparison with the experiments are described in section 3.3. In the conclusion section, the main results are summarized and some future directions of research are suggested.

2. Materials and Methods

2.1. Experimental setup for topotomography

A plate made of Al-Li 2.5% wt purchased from MaTeck was rolled to 45 % reduction and recrystallized 20 minutes at 530 °C to tune the grain size at 100 μm. The material was aged 4 hours at 100 °C to form very small Al_3Li precipitates with an expected size of 8 nm [22]. Small tomographic tension specimens (0.5 mm $\times$ 0.5 mm cross section) were cut using EDM in the middle of the plate for the experiment. The specimen geometry features a small stress concentration in the middle of the gage length and ensures that the first plastic events will occur in the observed region.

The experiment was carried out at the material science beam line (ID11) at the ESRF. The X-ray beam was produced by an in-vacuum undulator, and collimated to a size of about 0.7 x 0.7 mm by means of a X-ray transfocator [23]. The beam energy was set to 40 keV with a relative bandwidth of 3×10^{-3}. The diffractometer installed on ID11 has been designed for this particular variant of diffraction imaging experiments, which requires the alignment of a scattering vector parallel to the tomographic rotation axis [24,25]. The scattering vector $\underline{\boldsymbol{G}}$ is defined as $\underline{\boldsymbol{G}} = \underline{\boldsymbol{K}} - \underline{\boldsymbol{X}}$ with $\underline{\boldsymbol{X}}$ the incident wave vector and $\underline{\boldsymbol{K}}$ the diffracted wave vector, both with a norm of $1/\lambda$. Let us call (p, q, r) the components of the scattering vector $\underline{\boldsymbol{G}}_s$ expressed in the sample coordinate system for a set of (hkl) planes:

$$\underline{\boldsymbol{G}}_s = \boldsymbol{g}^{-1}\boldsymbol{B}\begin{pmatrix} h \\ k \\ l \end{pmatrix} = \begin{pmatrix} p \\ q \\ r \end{pmatrix} \tag{1}$$

where $\boldsymbol{g}$ is the orientation matrix of the crystal and $\boldsymbol{B}$ accounts for the lattice geometry (for cubic structures like Aluminium it reduces to the lattice parameter times the identity).

Following [26,27] and accounting for the four diffractometer rotation angles (Θ, ω, ϕ, χ), via the four associated rotation matrices[1] ($\boldsymbol{T}$, $\boldsymbol{\Omega}$, $\boldsymbol{\Phi}$, $\boldsymbol{X}$), the Bragg diffraction condition in 3D can be written as:

$$\frac{2\sin^2(\theta_{Bragg})}{\lambda} = -\left[\boldsymbol{T}\boldsymbol{\Omega}\boldsymbol{\Phi}\boldsymbol{X}\begin{pmatrix} p \\ q \\ r \end{pmatrix}\right]_1 \tag{2}$$

In a topotomographic experiment the scattering vector is aligned with the rotation axis of the tomographic rotation stage ω (see Fig. 1a). For a known crystal structure and orientation (i.e. $\boldsymbol{B}$ and $\boldsymbol{g}$ are known), it is straightforward to rework Eq. (2) to derive the two tilt rotation values (χ, ϕ) :

$$\chi = \arctan\left(-\frac{p}{r}\right) \tag{3}$$

$$\phi = \arctan\left(\frac{q}{-p\sin(\chi) + r\cos(\chi)}\right) \tag{4}$$

Eq. (2) is then fulfilled for all possible values of ω. Note that in the DCT case, $\boldsymbol{T}$, $\boldsymbol{\Phi}$ and $\boldsymbol{X}$ vanish and the equation is only verified for 2 particular values, solutions of a quadratic equation in ω known as the rotating crystal problem.

---

[1] the rotation matrix $\boldsymbol{X}$ associated with the diffractometer angle χ should not be confused with the incident wave vector $\underline{\boldsymbol{X}}$

Preprints (www.preprints.org) | NOT PEER-REVIEWED | Posted: 10 September 2018 doi:10.20944/preprints201809.0179.v1

Peer-reviewed version available at Materials 2018, 11, 2018; doi:10.3390/ma11102018

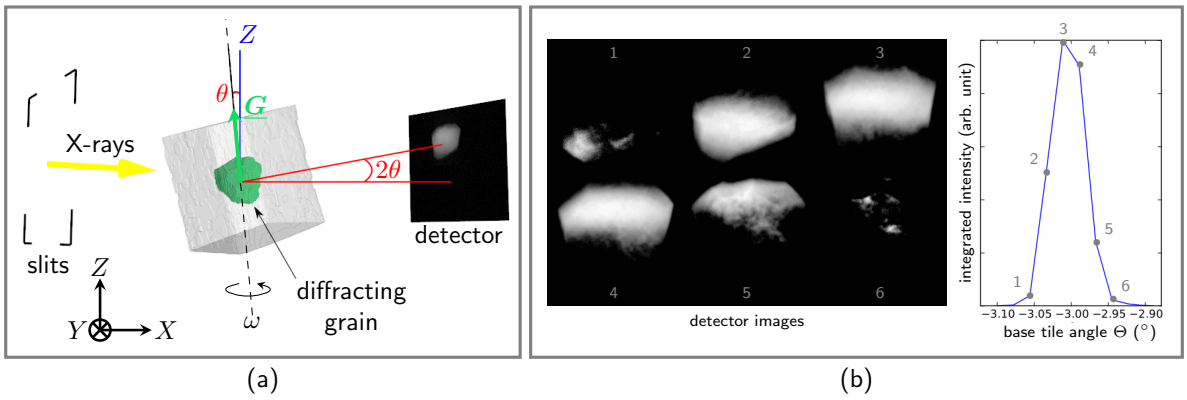

Figure 1. Schematics of the topotomographic alignment, (a) a scattering vector is aligned with the rotation axis and tilted by the nominal value $\Theta = \theta_{Bragg}$; (b) example of integrated detector intensity to build the rocking curve.

It is important to clearly understand the difference between Θ and θ_{Bragg} as they differ in nature. Θ is the value of the tilt applied by the base tilt motor, whereas θ_{Bragg} is a material parameter associated to a given d_{hkl} spacing and wavelength λ: $\theta_{Bragg} = \arcsin \lambda/2d$.

Now, in the ideal case of a perfect crystal and and quasi-monochromatic plane wave illumination, the entire grain would diffract for the position of the base tilt $\Theta = \theta_{Bragg}$, and only a simple rotation around ω would be needed to collect the topotomographic data set (see Fig. 1a). This is in practice never the case, as the inner mosaicity of the grain and dispersion effects requires to rock the base tilt (this is again a rotating crystal problem, which is covered in more details in section 2.5). A topotomographic (TT) data set can therefore be seen as a collection of rocking curves and associated stacks of 3D projection data and can be used in two different ways. First, *integrated* projection topographs corresponding to projections of the entire crystal volume are obtained by summing the intensity over the base tilt Θ. Inspection of these topographs allows for direct identification of the presence of crystalline defects such as the activation of slip systems (see Fig. 1b). Second, the width of the rocking curve $I = f(\theta)$ for a given ω position is a measure of the lattice rotation around the base tilt axis (Y here, see Fig. 1c).

2.2. Details of the in situ experiment

A small tomographic tension specimen was mounted in the Nanox stress rig, specifically designed to be compatible with both DCT and Topotomography acquisition geometries [15], see Fig. 3 left. The machine has a very limited size and weight and, thanks to the load bearing quartz tube, allows 360° visibility in DCT configuration with the detector as close as 3 mm to the rotation axis. Full visibility is also achieved in TT configuration with $\theta_{Bragg} \leq 10°$, with the detector as close as 10 mm from the rotation axis, for the complete range of motion of the two inner diffractometer circles ($\pm 20°$ and $\pm 15°$ for Φ and χ, respectively) [2].

With the specimen inside the stress rig, it is possible to analyze the initial undeformed bulk microstructure by a DCT scan. The DCT data is then processed to extract all grain orientations and positions within the gage length. Later on, the DCT reconstruction is also used as input to perform 3D CPFEM calculations (see section 2.3). For now, this data is used to select a series of grains for further analysis using topotomography imaging during mechanical loading. Here the selection was based on the following criteria: (i) a low order reflection must be accessible (note that the two circles Φ, χ used for the topotomographic alignment only have a limited range of motion), (ii) the grain must be located

[2] For given values of θ_{Bragg}, Φ and χ it is possible to move the TT detector even closer but this has to be checked manually

Preprints (www.preprints.org) | NOT PEER-REVIEWED | Posted: 10 September 2018 doi:10.20944/preprints201809.0179.v1

Peer-reviewed version available at Materials 2018, 11, 2018; doi:10.3390/ma11102018

in the bulk of the specimen, (iii) all the selected grains must form a small neighborhood. Grains number 4, 10 and 18 (see Fig. 2), located in the central region of the specimen, fit these constraints and were selected for the present study to carry out a series of topotomographic scans during an (interrupted) tensile test, see Fig. 3 right.

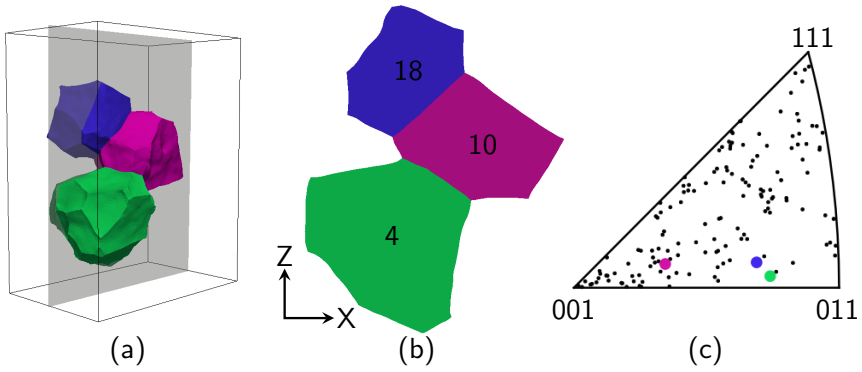

Figure 2. Details on the 3 grains cluster (a) 3D visualization of the grains (b); XZ slice through the 3 grains, (c) inverse pole figure of the gage length with the 3 grain orientations of interest highlighted.

At each of the 25 load steps, a phase contrast tomography of the gage length (1.5 mm in height) is also recorded and used to extract macroscopic strain information. The essential informations (grain orientation, aligned *hkl* reflection, Bragg angle, diffractometer angles) for each grain are reported in Tab. 1. Grains 10 and 18 have a similar orientation as seen on Fig. 2c).

Table 1. Details of the 3 grains selected for TT imaging, the orientation convention is consistent with [28] and angles values are given in °.

grain id	Orientation (Rodrigues)	aligned reflection	θ_{Bragg}	(Φ, χ) values
4	[0.050, -0.305, 0.104]	(202)	6.21	(0.52, -11.04)
10	[-0.028, -0.145, 0.062]	(002)	4.39	(2.14, 16.63)
18	[-0.135, -0.272, -0.333]	(202)	6.21	(-4.81, -12.88)

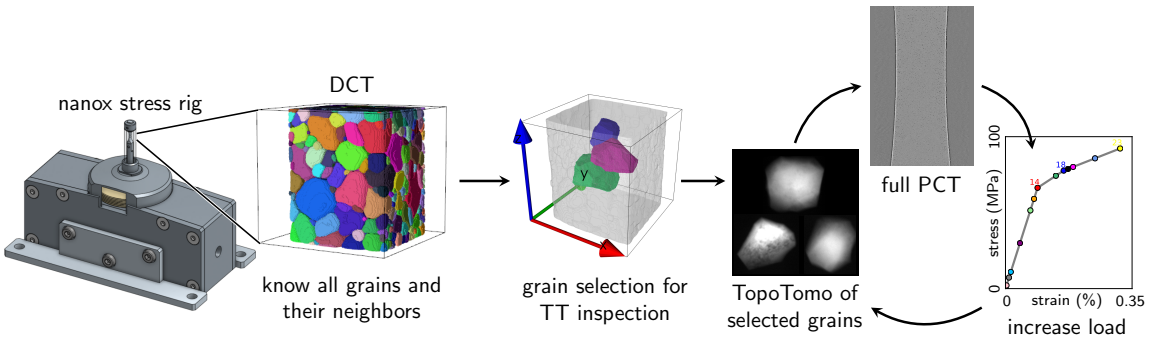

Figure 3. Sequence of the in-situ topotomography experiment: the initial microstructure is characterized by DCT and analyzed after mounting the specimen into the nanox device [29], then 23 complete sequences, each comprising three topotomography and one phase contrast tomography scan have been recorded at increasing levels of load (the color code used in the tension curve is used later on to plot results at a given load level).

Peer-reviewed version available at Materials 2018, 11, 2018; doi:10.3390/ma11102018

DCT scans were composed of 3600 equally spaced projections over 360°, recorded on a high-resolution detector with a transparent luminescent screen optically coupled by a 10× microscope objective to a 2048 × 2048 pixel ESRF Frelon camera, giving an effective pixel size of 1.4 μm. The same camera was used to record the PCT scans. A second detector system with a 20× objective and an effective pixel size of 0.7 μm was used for topotomographic scan acquisition. The angular range of the rocking curve scans was automatically adjusted after each load increment in order to cover the entire width of the crystal reflection curve for any ω rotation position of the sample. Moreover, the X-ray flux density was further increased by focusing the beam on the area covered by the 3 grain cluster. A continuous motion acquisition procedure with a fixed integration range of 0.1° and 0.5 s exposure time per image was used. Integration gaps caused by the readout time of the CCD detector could be eliminated by operating the system in frame transfer mode[3]. This procedure was repeated every 4° and a complete topotomographic acquisition comprising 90 such rocking scans per grain typically lasted from 10 minutes up to an hour as the Θ integration range increased during loading.

2.3. Crystal Plasticity Finite Element Simulations

A finite strain crystal plasticity model, fully described in [30] is used here to compute the mechanical response of the polycrystalline sample under tension. It is based on the multiplicative decomposition $\underset{\sim}{\mathbf{F}} = \underset{\sim}{\mathbf{E}}\underset{\sim}{\mathbf{P}}$ of the deformation gradient, $\underset{\sim}{\mathbf{F}}$, into an elastic part, $\underset{\sim}{\mathbf{E}}$, and a plastic part, $\underset{\sim}{\mathbf{P}}$. The multiplicative decomposition is associated with the definition of an intermediate configuration for which the elastic part of the deformation gradient is removed. The intermediate released configuration is uniquely determined up to a rigid body rotation which is chosen such that the lattice orientation in the intermediate configuration is the same as the initial one. [Mandel, 1973a] called it the isoclinic intermediate configuration. As a result, lattice rotation and distortion during elastoplastic deformation are contained in the elastic deformation part $\underset{\sim}{\mathbf{E}}$. The transformation $\underset{\sim}{\mathbf{E}}$ has a pure **rotation** part $\underset{\sim}{\mathbf{R}}^e$ and a pure **distortion** part $\underset{\sim}{\mathbf{U}}^e$ which can be obtained by the polar decomposition:

$$\underset{\sim}{\mathbf{E}} = \underset{\sim}{\mathbf{R}}^e \underset{\sim}{\mathbf{U}}^e \tag{5}$$

Plastic deformation is the result of slip processes according to a collection of N slip systems, each one characterised by the slip direction $\underline{\boldsymbol{m}}^s$ and the normal to the slip plane $\underline{\boldsymbol{n}}^s$. In the intermediate configuration:

$$\dot{\underset{\sim}{\mathbf{P}}}\underset{\sim}{\mathbf{P}}^{-1} = \sum_{s=1}^{N} \dot{\gamma}^s \underline{\boldsymbol{m}}^s \otimes \underline{\boldsymbol{n}}^s \tag{6}$$

In order to analyze the microplastic behavior of the studied AlLi polycrystal, an elastovisco-plastic crystal plasticity model was selected. Numerical computations were performed using the Z-set software[4] (see [31]). The slip rate on a given slip system s depends, via a power law, on how much the resolved shear stress τ^s exceeds the threshold $\tau_0 + r^s$:

$$\dot{\gamma}^s = \left\langle \frac{|\tau^s| - \tau_0 - r^s}{K} \right\rangle^n \mathrm{sign}(\tau^s) \tag{7}$$

Here, τ_0 is the critical resolved shear stress and r^s, initially zero, increases with increasing plastic strain and hardens the system s through a non-linear isotropic hardening rule, as developed in [32]:

---

[3] in frame transfer mode only half of the active area is available for image acquisition whilst the other half is used for temporary storage and readout of the previous frame

[4] http://www.zset-software.com

Preprints (www.preprints.org) | NOT PEER-REVIEWED | Posted: 10 September 2018 doi:10.20944/preprints201809.0179.v1

Peer-reviewed version available at Materials 2018, 11, 2018; doi:10.3390/ma11102018

$$r^s = Q \sum_{r=1}^{N} h^{sr}(1 - \exp(-bv^s)) \tag{8}$$

v^s is the cumulative slip and h^{sr} denotes the interaction matrix taking into account the relative influence of slip systems on each other. It includes the self and latent hardening, and only indirect and estimated quantitative information is available about the components of this matrix (see for instance [33,34]).

Monotonic tensile tests were performed on five different macroscopic samples, at three strain rates and a numerical optimization using Z-set implementation was performed to find a suitable parameter set (τ_0, Q, b), as presented in Table 2. The material exhibits an inverse strain rate sensitivity of the yield stress which prevented to identify K and n, instead sensible values for aluminium alloys have been used. Modelling this effect requires a more complex model including dynamic strain ageing as in [35]. For the interactions between dislocations, coefficients h^{rs} from [36] have been used.

Table 2. Material parameters identified from the macroscopic tensile tests.

K (MPa$^{1/n}$)	n (-)	τ_0 (MPa)	Q (MPa)	b (-)
38	10	10	5.3	763

The experimental grain map is used as input to produce a high fidelity digital clone of the specimen. The entire $L = 1.57$ mm zone, where 3 DCT scans were merged, was used to ensure the boundary condition application is far enough from the grains of interest to avoid any boundary layer effect [37]. Details on how the mesh was produced can be found in [17]. The initial grain boundary surface generated contains a very large number of triangles and an iterative decimation approach using an edge collapsing algorithm is applied. The surface mesh is filled with tetrahedra controlling the mesh density as a function of the euclidean distance d from the three grain cluster. This allowed minimizing the computational cost while preserving a rich description of the mechanical fields in the region of interest. The final mesh is composed of 341687 linear tetrahedra with a gradient in element size (the ratio between the maximum and minimum tetrahedron size is about 4000) visible on Fig. 4.

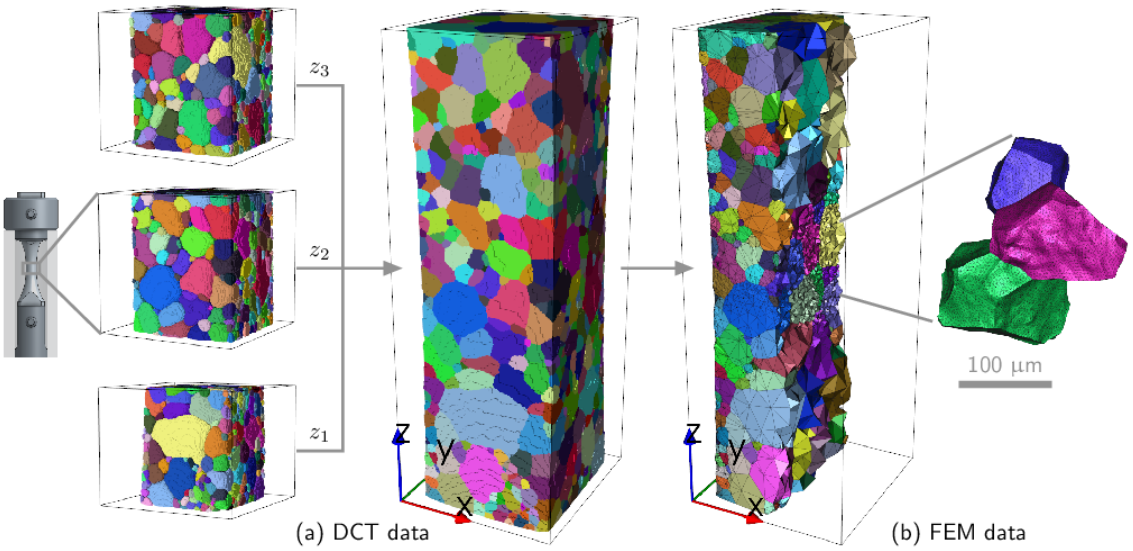

Figure 4. Comparison between the DCT data (a) and the mesh generated (b); the colors denote the grain numbers which are consistent from the experiment to the simulation.

Dirichlet boundary conditions ($u_z = 0$ on the lower face and $u_z = 15.7$ microns on the upper face) were imposed to deform the specimen in tension up to 1% total strain in 100 steps. Suitable boundary conditions have been set on the lower surface of the sample to prevent any rigid body motion and lateral surfaces were free of stress. The steps corresponding to the experimentally measured strain (for instance 0.32% total strain) can be used for comparison.

2.4. Lattice rotations

The continuum mechanical approach used here makes it possible to distinguish between the transformation of material and lattice directions. Material lines are made of material points that are subjected to the motion field $\boldsymbol{u}$. In contrast, lattice directions are not material insofar as they are not necessarily made of the same material points (atoms) in the initial and current configurations due to the passing of dislocations, but keep the same crystallographic meaning. According to the concept of isoclinic configuration, lattice directions are unchanged from the initial to the intermediate configuration. Dislocations passing through a material volume element do not distort nor rotate the lattice, although material lines are sheared. According to the continuum theory of dislocations, statistically stored dislocations accumulating in the material volume element affect material hardening but do not change the element shape. Accordingly, an initial lattice direction $\underline{\boldsymbol{d}}^{\sharp}$ is transformed into $\underline{\boldsymbol{d}}$ by means of the elastic deformation:

$$\underline{\boldsymbol{d}} = \underset{\sim}{\mathbf{E}}.\underline{\boldsymbol{d}}^{\sharp} \tag{9}$$

This important distinction allows to precisely compute the local rotation and distortion of the crystal lattice and further derive the 3D rocking curve of a grain from its deformed state in the simulation (see 2.5).

2.5. Rocking curves simulations from CPFEM data

As explained in section 2.1, the rocking curve represents the intensity diffracted by the illuminated grain at a given Θ angle. As soon as the crystal deforms, the exact Bragg condition is violated and the $I(\Theta)$ curve will widen. In crystal plasticity, geometrically necessary dislocations (GND) give rise to gradients of crystal orientation, leading to local modification of the Bragg condition. The problem is therefore to solve the 3D diffraction condition stated in Eq. 2 for the angle Θ, with a locally deformed crystal lattice. In Eq. 2, the values of (p, q, r) as well as θ_{Bragg} need to be updated for the new lattice geometry. It is therefore possible to use the mechanical fields computed in each element (namely $\underset{\sim}{\mathbf{E}}$ and $\underset{\sim}{\mathbf{R}}^{e}$) to evaluate locally the Bragg condition (for a given ω value) and to find the corresponding Θ. Building the volume weighted histogram for all elements within the grain will produce a simulated rocking curve (for this value of ω).

3. Results

3.1. Topography results

X-ray topographs are 2D oblique projections of a crystal. At the onset on plasticity, slip system activity may modify the local Bragg condition within the grain and produce orientation contrasts on the detector. In this section, topographs over a full ω turn for three neighboring grains as a function of the load, are analysed.

As we shall see, the perturbations of the crystal lattice are localised within the slip plane, and may only be visible at certain ω angles, called edge-on configuration, when the diffraction direction is contained in the plane (ie the tilted slip plane normal $\underline{\boldsymbol{n}}_t$ is perpendicular to $\underline{\boldsymbol{K}}$). Knowing the grain

orientation and the tilt geometry, it is straightforward to obtain the 2 edge-on ω angles for a given slip plane by solving[5]:

$$(\mathbf{\Omega}.\underline{\boldsymbol{n}}_t).\underline{\boldsymbol{K}} = 0 \quad \text{with} \quad \underline{\boldsymbol{K}} = \frac{1}{\lambda}\begin{pmatrix}\cos(\theta_{Bragg})\\ 0\\ \sin(\theta_{Bragg})\end{pmatrix} \tag{10}$$

This means solving $[n_t[0]\cos(\omega) - n_t[1]\sin(\omega)]\cos(\theta) + n_t[2]\sin(\theta) = 0$. The two ω values, for a given slip plane, are separated by close to 180°, a value depending on θ_{Bragg}.

Table 3 gathers the ω values for the two slip systems with the highest Schmid factor in the 3 grains calculated with Eq. (10). These values will be used to show the topographs in edge-on configuration where the contrast is expected to be maximal for a given slip plane. Note that the values for the two observed slip planes (not to be confused with the two values for a given slip plane) are exactly separated by 180 degrees. For grains 4 and 18, the aligned reflection is (202); and rotating around this axis, the edge-on configurations for the slip planes with the two highest Schmid factors $(1\bar{1}1)$ and (111) are 180° apart (they share the $[\bar{1}01]$ zone axis which is perpendicular to the scattering vector). For grain 10, the aligned reflection is (002); rotating around this axis the edge-on configurations for the (111) and $(11\bar{1})$ planes are also 180° apart (they share the $[\bar{1}10]$ zone axis which is perpendicular to the scattering vector).

Table 3. Edge-on ω values for the two slip systems with the highest Schmid factor in the 3 grains; ω values in bold are used to show the topographs in edge-on configuration in Fig. 5.

grain id	(hkl)	Schmid factor	(ω_1, ω_2)
4	(1-11)	0.476	(338.6, **176.3**)
	(111)	0.461	(158.6, 356.3)
10	(111)	0.490	(214.5, **40.8**)
	(1-11)	0.473	(304.5, 130.8)
18	(111)	0.488	(209.1, 46.8)
	(1-11)	0.457	(**29.1**, 226.8)

Integrated topographs at the recorded ω closest to the edge-on values and for selected load levels are shown in Fig. 5. Contrast forming bands within the grains is clearly visible and appear first for grain 10, then grain 18 and finally for grain 4.

[5] Here we do not account for the base tilt as both left and right side of the equation would be equally affected.

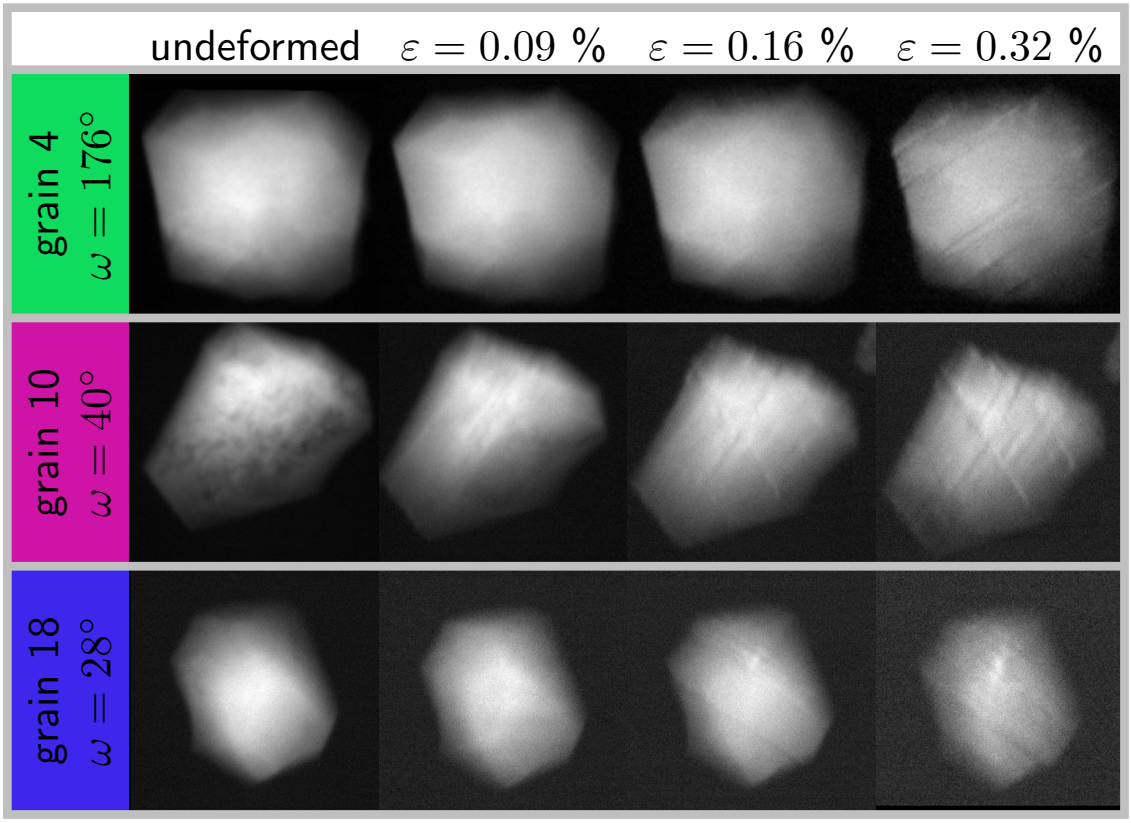

Figure 5. Integrated topographs over Θ in edge-on configuration for each grain of the cluster and different load levels; videos of the complete ω set are avaiable as supplementary material for grain 4 in the initial and deformed states.

These sets of bands are parallel, most of the time extend through the whole grain and their number increases as the deformation increases. Going through the whole projection set for each grain shows that 2 sets of bands are visible at different ω values. For grain 10, the crystallographic configuration is such that both sets are visible at around 40°. This is, to the best of the author knowledge, the first in situ observation of bulk plasticity in a millimeter sized polycrystalline specimen. From there, the orientation of the bands, their number and location within the grain can be further studied.

Preprints (www.preprints.org) | NOT PEER-REVIEWED | Posted: 10 September 2018 doi:10.20944/preprints201809.0179.v1

Peer-reviewed version available at Materials 2018, 11, 2018; doi:10.3390/ma11102018

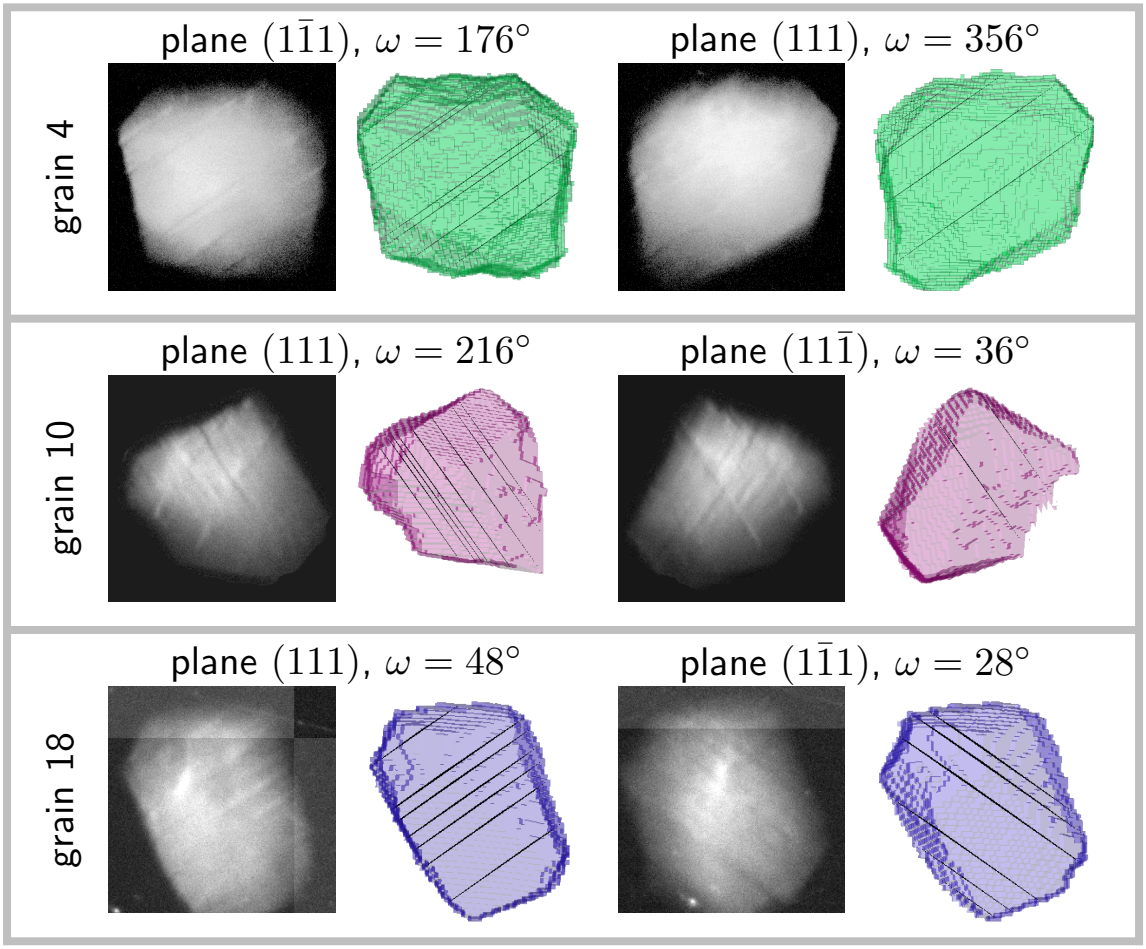

Figure 6. Identification of the bands as slip plane traces visible in the edge-on geometrical configuration in the topographs; here the two observed active slip planes are shown for one of the two ω angle; the active slip plane locations within the grains have been measured manually and displayed in 3D.

Using the initial grain orientation and the tilt geometries for each aligned reflection, it is possible to correlate the angle of those bands to specific crystallographic planes (see Fig. 6). For this, a 3D geometrical representation[6] of the grain was built using the DCT reconstruction and the relevant slip planes have been added inside according to the measured grain orientation. The grain can be tilted in the topotomographic condition and rotated to the given edge-on omega angle. Using a parallel projection mode and setting the view in the diffracted beam direction $\underline{\boldsymbol{K}} = (1, 0, \tan(2\theta_{Bragg}))$ produces the same conditions as when collecting the topographs. All the observed bands have been identified without any ambiguity as projections of {111} planes, see Fig. 6. In each case the exact slip plane could be identified and further related to the Schmid factor. This demonstrates that the onset of plasticity, from the first slip band to the more advanced state where several slip systems are active, was indeed captured in situ during this experiment.

[6] The open source library pymicro was used to this end https://github.com/heprom/pymicro

For grain 4 and 18, the two observed slip planes correspond to the two highest Schmid factors (see Tab. 3) whereas for grain 10, they correspond to the first and third highest Schmid factors. The slip system corresponding to the second highest Schmid is not observed to be active in this grain.

Rocking curves are presented in Fig. 7, for each grain at the strain levels and for the same ω values as in Fig. 5. All 3 grains exhibit a consistent behavior, with a narrow curve at the beginning which first shifts to the lower $|\theta_{Bragg}|$ values due to elastic loading (increase of the d_{hkl} interplanar spacing) and then widens considerably when plasticity takes place.

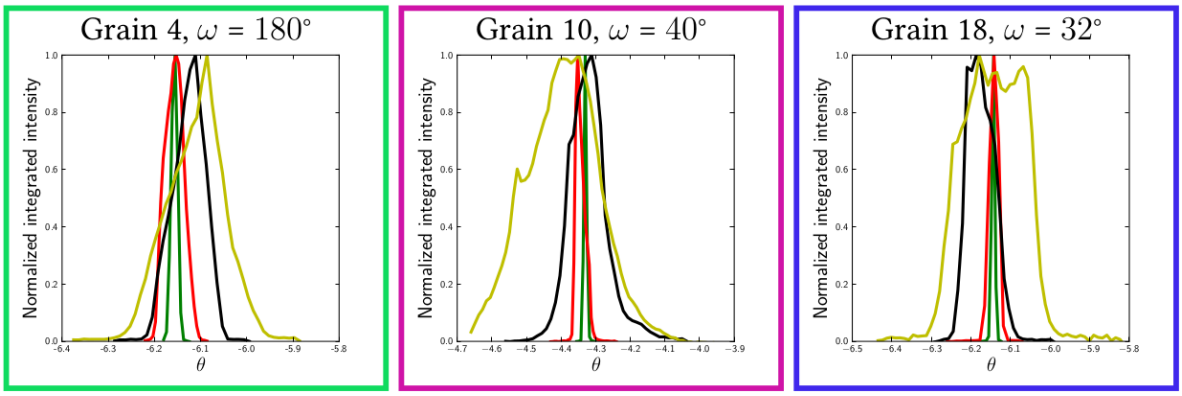

Figure 7. Evolution of the rocking curves for each grain of the cluster during in situ loading, the curve colors refer to the load levels in Fig. 5.

3.2. 3D rocking curves results

As grains are aligned in a topotomographic sense, it is possible to measure rocking curves at every ω position. This measure is therefore sensitive not only to the amount of curvature of a crystal but also to the orientation of this curvature in real space. To quantify the intragranular orientation spread revealed by a rocking curve, we introduce the width of the RC at 10% of the peak of the normalized intensity, denoted as FWEM - Full Width of the Effective Misorientation. Although the effective misorientation describes the change in Bragg condition due to both orientation and lattice spacing variations; in practice, the orientation effect is largely predominant. Therefore, this value is a direct (qualitative) measure of the orientation spread, around the axis defined by the base tilt.

The FWEM was measured every 4° (for each ω position) and is plotted at all different load levels in Fig. 8 to observe its evolution with increasing plasticity. An interesting dumbell shaped curve is consistently obtained for the 3 grains. The curve widens in a preferential direction linked to the active slip systems within the grain. One can observe that the FWEM is similar for grains 4 and 18 which have the same combination of active slip systems. The orientation of the curves for grain 10 is different and exhibits a clear reorientation of the preferential direction towards the end of the loading sequence. This may be linked to changes in the relative activity of the dominant slip system(s) during deformation but would require further analysis.

The shape of the curve can be understood more clearly considering the idealized case of a strain free crystal bent by an amount $\Delta\Theta$ by geometrically necessary dislocations. In the kinetic approximation this configuration would produce a figure made of two tangent circles giving a vanishing FWEM in the bending axis direction (no lattice rotation) and of exactly $\Delta\Theta$ perpendicular to it. The FWEM can be seen as the limit of the Bragg condition when rocking the base tilt Θ and can be computed using the rotating crystal equation solving for Θ for a known ω (see Fig. 8 bottom right).

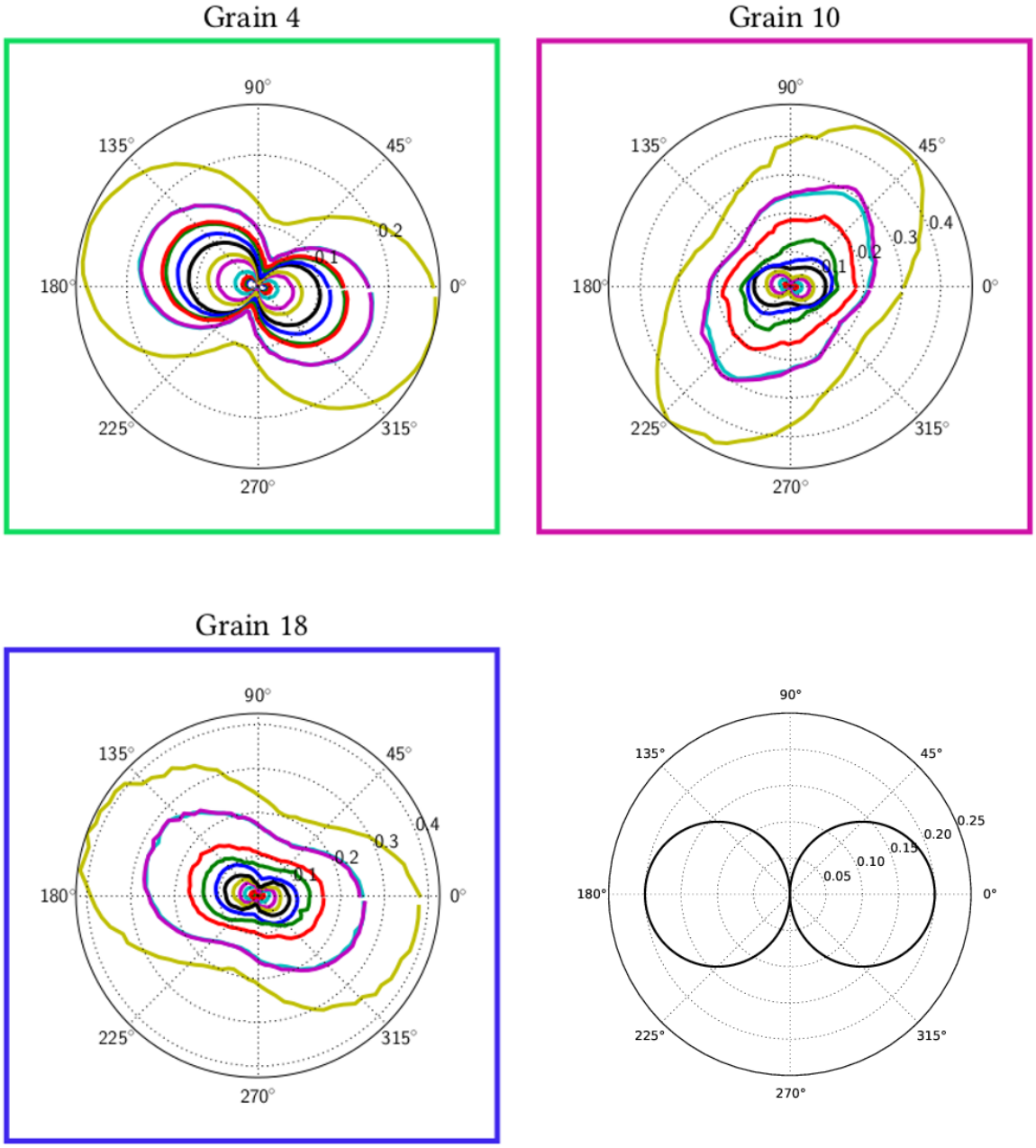

Figure 8. In-situ FWEM as a function of ω, for each grain of the cluster (the color code matches the one used for the tensile curve in Fig. 3), and example of the FWEM in the case of a crystal ideally bent around a single axis by 0.2° (bottom right).

3.3. Comparison with CPFEM simulations

The first comparison is the slip activity computed with the numerical model for each grain with the activity visible on the topographs for a particular ω position (see section 3.1). The CPFEM simulations give access to the active slip systems as opposed to the slip planes only which were identified experimentally on the topograph. The slip activity is captured by averaging the amount of slip for a given slip system within the grain and can be compared to the qualitative information obtained on the topographs (intensity of the contrast and number of bands).

Accumulated plasticity (all slip system contributions) within the bulk is shown on Fig. 9a and the slip activity for each of the 3 grains is detailed in Fig. 9b. For grains 4 and 18, which have close orientations and behave similarly the model predicts double slip with systems (111)[0-11] and

Preprints (www.preprints.org) | NOT PEER-REVIEWED | Posted: 10 September 2018 doi:10.20944/preprints201809.0179.v1

Peer-reviewed version available at Materials 2018, 11, 2018; doi:10.3390/ma11102018

(1-11)[011] just as observed experimentally and no other slip activity. The situation is different in grain 10 which also showed double slip experimentally but with planes (111) and (11-1), whereas the model predicts plastic activity on 3 planes (111), (1-11) and (11-1). It is interesting to see that despite the general agreement, the details of the slip system activation are far from perfect. The discrepancy may be attributed to parameters of the constitutive laws especially regarding the interaction matrix coefficients h^rs. These parameters were determined from macroscopic tensile curves and from literature. A detailed parametric study is necessary to analyze the impact of these parameters values on the activation of slip systems in that grain. This can be seen as an opportunity to use such experimental data collected at the length scale of the grains and in the bulk to enrich identification data sets and solve the long standing issue of crystal plasticity material parameter identification [38].

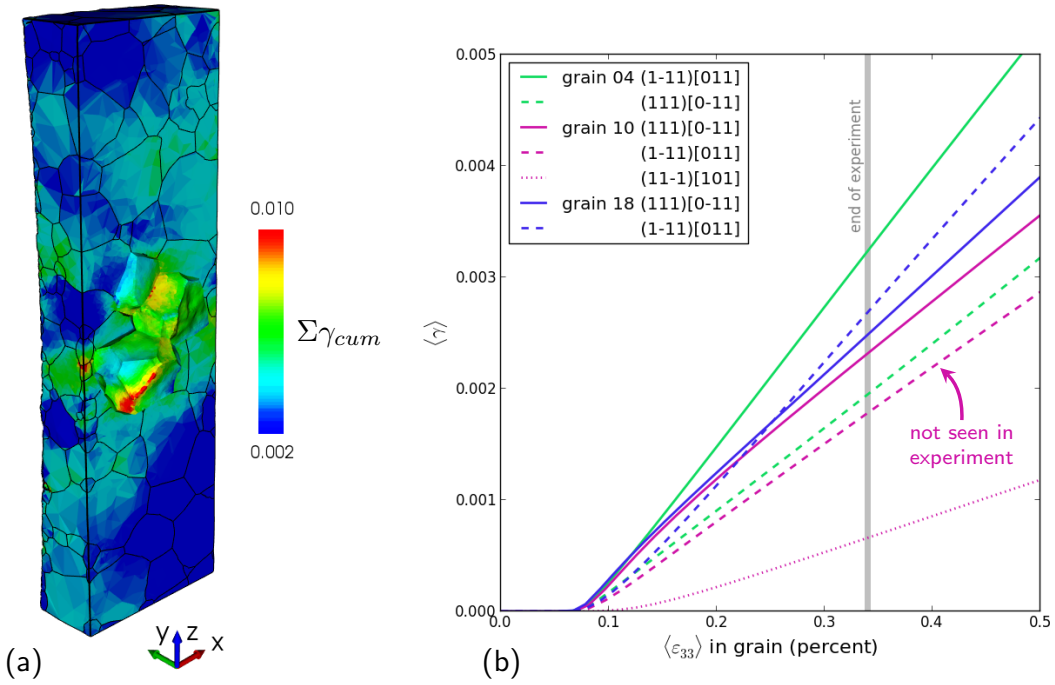

Figure 9. Predicted plastic activity (a) view of the interior of the specimen showing the accumulated plasticity at the load level corresponding to the end of the experiment (b) average plastic activity in the 3 grains of the cluster, the most active slip system is represented with a solid line and the second most active with a dashed line, the grain color code is used.

Using the simulated mechanical fields within the grains, rocking curves can be simulated as described in section 2.5. The generated rocking curves for each grain of the cluster are plotted in Fig. 10, at $\omega = 165°$. The obtained behaviour is consistent with the experimental observations. The rocking curve first shifts to lower Θ values due to the increase of the interplanar distance during loading. A very small amount of broadening due to the heterogeneous elastic strain field within the grain is also observed. When plasticity kicks in and slip systems start to be active, the curve widening is more pronounced, and the shape changes which can be related to the tendency to form subgrain-like regions. This effect has been studied both theoretically and experimentally for instance by [39–41].

Preprints (www.preprints.org) | NOT PEER-REVIEWED | Posted: 10 September 2018 doi:10.20944/preprints201809.0179.v1

Peer-reviewed version available at Materials 2018, 11, 2018; doi:10.3390/ma11102018

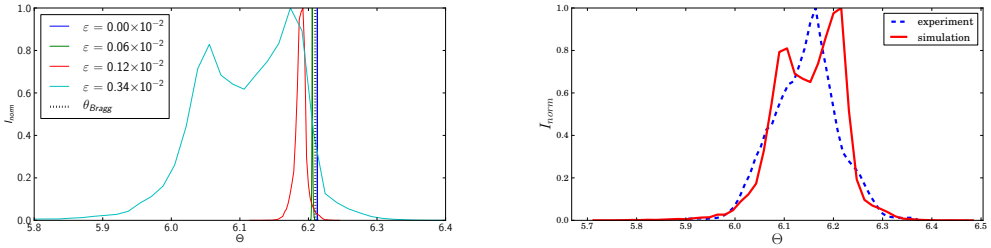

Figure 10. (a) Simulated rocking curves for grain 4 at $\omega = 165°$ at four different strain levels; (b) Comparison between experimental simulated rocking curves at $\varepsilon_{33} = 2 \times 10^{-4}$.

Finally a quantitative comparison between experimental FWEM and synthetic FWEM is presented in Fig. 11. Synthetic curves are plotted for an applied strain of $\varepsilon_{33} = 0.0034$, and experimental surfaces are plotted for the last step of the topotomography experiment. Both curves are in very good agreement for grain 4 and grain 18, for both shape and orientation. For grain 10, the surface has the right amplitude but not the right direction. As explained previously, the direction of the dumbbell shaped curve is linked to the precise combination of active slip systems within the grain and the discrepancy between the predicted and observed slip systems is presumably the cause of the mismatch in orientation for this case.

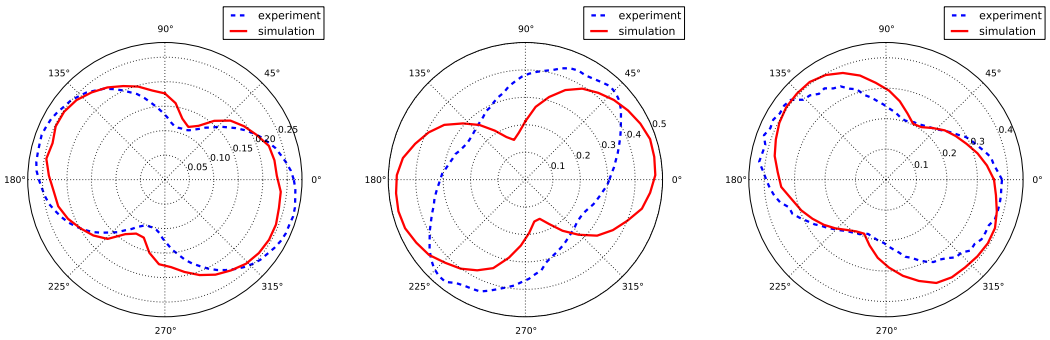

Figure 11. Comparison between experimental simulated FWEM at $\varepsilon_{33} = 2 \times 10^{-4}$ for the 3 investigated grains.

4. Conclusions

An in-situ topotomographic experiment has been carried out at a synchrotron facility to collect a very detailed 4D dataset to study the onset of plastic slip under tension in an Aluminium Lithium alloy. Initial DCT imaging allowed to measure the initial microstructure and to select a set of 3 grains in the bulk of the specimen for further investigations. Upon loading, incipient plasticity was observed non destructively in the form of band contrast in X-ray topographs, which were further related geometrically to active slip planes in the bulk.

Information collected from rocking curves was presented in the form of polar plots illustrating the anisotropy of mean lattice curvature. The polar plots have a characteristic dumbbell shape which can be attributed to lattice bending with respect to some specific axis which could be determined in the experiment for the 3 grains during deformation.

Crystal plasticity simulations were carried out to compare the prediction obtained with a classical continuum model with our experimental observations. Essential features, such as slip system activation and average misorientation per grain are well captured by the model although some discrepancies remain for one grain. A major contribution of the work is the comparison of experimental and simulated misorientation polar plots showing characteristic dumbbell shapes quantifying the anisotropy of lattice curvature.

A striking feature of the presented experiment is the direct observation of inelastic deformation mechanisms in the bulk (plastic slip, but also twinning or phase transformation are possible). The detected slip system activity could be used in the material parameter identification procedure instead of macroscopic tests only. This would require a specific treatment (for instance using grain averaged quantities) since the full field calculation is costly and not well suited for an optimization routine.

One of the limitations of the present work is that only one specimen could be tested in the given beam-time. Building on this experiment, and using the developed automation algorithms, future work will target more specimens and more grains per specimen to obtain more statistics and study slip transmission in more detail.

The adaptation of advanced reconstruction techniques [13] to this type of combined DCT and Topotomography acquisitions might allow to retrieve finer details of the orientation fields and their evolution at increasing levels of applied strain. This could be used to study more complex inelastic mechanisms in metals or to extract more dependable constitutive parameters minimizing the discrepancies between experimental observations and numerical simulations on the digital twins of the tested specimen.

Supplementary Materials: The following are available online at www.mdpi.com/link, Video S1: Full set of integrated topographs over 360 degrees (every 4°) for grain 4 in the undeformed state, Video S2: Full set of integrated topographs over 360 degrees (every 4°) for grain 4 in the deformed state.

Acknowledgments: MINES Paristech is acknowledged for funding the PhD of NG; the authors thank the ESRF for providing the beam time for this experiment under proposal MA2285.

Author Contributions: "H.P. and W.L. conceived and designed the experiments; N.G. W.L. and H.P. performed the experiments; N.G. and H.P. analyzed the data; S.F. contributed the crystal plasticity model; N.G. ran the simulations; H.P. and N.G. wrote the paper; W.L and S.F. provided comments on the manuscript."

Conflicts of Interest: The authors declare no conflict of interest.

Abbreviations

The following abbreviations are used in this manuscript:

EDM: Electro-Discharge Machining DCT: Diffraction Contrast Tomography
TT: Topotomography
PCT: Phase Contrast Tomography
CPFEM: Crystal Plasticity Finite Element Method

References

1. Wilkinson, A.J.; Britton, T.B. Strains, planes, and EBSD in materials science. *Materials Today* **2012**, *15*, 366–376.
2. Chen, Z.; Daly, S.H. Active Slip System Identification in Polycrystalline Metals by Digital Image Correlation (DIC). *Experimental Mechanics* **2016**, pp. 1–13.
3. Stinville, J.; Echlin, M.; Texier, D.; Bridier, F.; Bocher, P.; Pollock, T. Sub-Grain Scale Digital Image Correlation by Electron Microscopy for Polycrystalline Materials during Elastic and Plastic Deformation. *Experimental Mechanics* **2016**, *56*, 197–216.
4. Roters, F.; Eisenlohr, P.; Hantcherli, L.; Tjahjanto, D.D.; Bieler, T.R.; Raabe, D. Overview of constitutive laws, kinematics, homogenization and multiscale methods in crystal plasticity finite-element modeling: Theory, experiments, applications. *Acta Materialia* **2010**, *58*, 1152–1211.
5. Signor, L.; Villechaise, P.; Ghidossi, T.; Lacoste, E.; Gueguen, M.; Courtin, S. Influence of local crystallographic configuration on microcrack initiation in fatigued 316LN stainless steel: experiments and crystal plasticity finite elements simulations. *Material Science and Engineering A* **2016**, *649*, 239–249.
6. Guan, Y.; Chen, B.; Zou, J.; Britton, T.B.; Jiang, J.; Dunne, F.P.E. Crystal plasticity modelling and HR-DIC measurement of slip activation and strain localization in single and oligo-crystal Ni alloys under fatigue. *International Journal of Plasticity* **2017**, *88*, 70–88.

7. Zeghadi, A.; N'Guyen, F.; Forest, S.; Gourgues, A.F.; Bouaziz, O. Ensemble averaging stress–strain fields in polycrystalline aggregates with a constrained surface microstructure–Part 1: Anisotropic elastic behaviour. *Philosophical Magazine* **2007**, *87*, 1401–1424.
8. Echlin, M.P.; Straw, M.; Randolph, S.; Filevich, J.; Pollock, T.M. The TriBeam system: Femtosecond laser ablation in situ SEM. *Materials Characterization* **2015**, *100*, 1–12.
9. Poulsen, H.F. An introduction to three-dimensional X-ray diffraction microscopy. *Journal of Applied Crystallography* **2012**, *45*, 1084–1097.
10. Borbély, A.; Kaysser-Pyzalla, A.R. X-ray diffraction microscopy: emerging imaging techniques for nondestructive analysis of crystalline materials from the millimetre down to the nanometre scale. *Journal of Applied Crystallography* **2013**, *46*, 295–296.
11. Ludwig, W.; King, A.; Reischig, P.; Herbig, M.; Lauridsen, E.; Schmidt, S.; Proudhon, H.; Forest, S.; Cloetens, P.; du Roscoat, S.R.; Buffière, J.; Marrow, T.; Poulsen, H. New opportunities for 3D materials science of polycrystalline materials at the micrometre lengthscale by combined use of X-ray diffraction and X-ray imaging. *Materials Science and Engineering: A* **2009**, *524*, 69–76. Special Topic Section: Probing strains and Dislocation Gradients with diffraction.
12. Ludwig, W.; King, A.; Herbig, M.; Reischig, P.; Marrow, J.; Babout, L.; Lauridsen, E.M.; Proudhon, H.; Buffière, J.Y. Characterization of Polycrystalline Materials Using Synchrotron X-ray Imaging and Diffraction Techniques. *JOM* **2010**, *62*, 22–28.
13. Viganò, N.; Tanguy, A.; Hallais, S.; Dimanov, A.; Bornert, M.; Batenburg, K.J.; Ludwig, W. Three-dimensional full-field X-ray orientation microscopy. *Scientific Reports* **2016**, *6*, 20618.
14. Schuren, J.C.; Shade, P.A.; Bernier, J.V.; Li, S.F.; Blank, B.; Lind, J.; Kenesei, P.; Lienert, U.; Suter, R.M.; Turner, T.J.; Dimiduk, D.M.; Almer, J. New opportunities for quantitative tracking of polycrystal responses in three dimensions. *Current Opinion in Solid State and Materials Science* **2015**, *19*, 235–244.
15. Guéninchault, N.; Proudhon, H.; Ludwig, W. Nanox, a miniature mechanical stress rig designed for near-field X-ray diffraction imaging techniques **2016**. *23*, 1474–1483.
16. Turner, D.M.; Kalidindi, S.R. Statistical construction of 3-D microstructures from 2-D exemplars collected on oblique sections. *Acta Mater.* **2016**, *102*, 136–148.
17. Proudhon, H.; Li, J.; Reischig, P.; Guéninchault, N.; Forest, S.; Ludwig, W. Coupling Diffraction Contrast Tomography with the Finite Element Method **2016**. *18*, 903–912.
18. McDowell, D.L.; Dunne, F.P.E. Microstructure-sensitive computational modeling of fatigue crack formation. *International Journal of Fatigue* **2010**, *32*, 1521–1542. Emerging Frontiers in Fatigue.
19. Miller, M.P.; Dawson, P.R. Understanding local deformation in metallic polycrystals using high energy X-rays and finite elements. *Current Opinion in Solid State and Materials Science* **2014**, *18*, 286–299.
20. Erinosho, T.; Collins, D.; Wilkinson, A.; Todd, R.; Dunne, F. Assessment of X-ray diffraction and crystal plasticity lattice strain evolutions under biaxial loading. *International Journal of Plasticity* **2016**, *83*, 1–18.
21. Guery, A.; Hild, F.; Latourte, F.; Roux, S. Identification of crystal plasticity parameters using DIC measurements and weighted FEMU. *Mechanics of Materials* **2016**, *100*, 55–71.
22. Brechet, Y.; Livet, F. LOW CYCLE FATIGUE OF BINARY Al-Li ALLOYS : III-COALESCENCE OF δ' PRECIPITATES IN FATIGUE : X-RAY LOW ANGLE SCATTERING INVESTIGATION. *Journal de Physique Colloques* **1987**, *48*, C3–717–C3–719.
23. X-ray transfocators: Focusing devices based on compound refractive lenses. *Journal of Synchrotron Radiation* **2011**, *18*, 125–133.
24. Ludwig, W.; Cloetens, P.; Härtwig, J.; Baruchel, J.; Hamelin, B.; Bastie, P. Three-dimensional imaging of crystal defects by 'topo-tomography'. *J. Appl. Cryst.* **2001**, *34*, 602–607.
25. Ludwig, W.; Lauridsen, E.M.; Schmidt, S.; Poulsen, H.F.; Baruchel, J. High-resolution three-dimensional mapping of individual grains in polycrystals by topotomography. *Journal of Applied Crystallography* **2007**, *40*, 905–911.
26. Busing, W.R.; Levy, H.A. Angle calculations for 3- and 4-circle X-ray and neutron diffractometers. *Acta Crystallographica* **1967**, *22*, 457–464.
27. Poulsen, H.F. *Three-Dimensional X-ray Diffraction Microscopy – Mapping Polycrystals and Their Dynamics*; Vol. 205, *Springer Tracts in Modern Physics*, Springer: Berlin, 2004.

28. Rowenhorst, D.; Rollett, A.D.; Rohrer, G.S.; Groeber, M.; Jackson, M.; Konijnenberg, P.J.; De Graef, M. Consistent representations of and conversions between 3D rotations. *Model. Simul. Mater. Sci. Eng.* **2015**, *23*, 083501.
29. Gueninchault, N.; Proudhon, H.; Ludwig, W. Nanox: a miniature mechanical stress rig designed for near-field X-ray diffraction imaging techniques. *Journal of Synchrotron Radiation* **2016**, *23*, 1474–1483.
30. Besson, J.; Cailletaud, G.; Chaboche, J.L.; Forest, S.; Blétry, M. *Non-Linear Mechanics of Materials*; Vol. 167, Springer Netherlands, 2010.
31. Besson, J.; Foerch, R. Large scale object-oriented finite element code design. *Computer Methods in Applied Mechanics and Engineering* **1997**, *142*, 165–187.
32. Meric, L.; Poubanne, P.; Cailletaud, G. Single Crystal Modeling for Structural Calculations: Part 1—Model Presentation. *Journal of Engineering Materials and Technology* **1991**, *113*, 162–170.
33. Franciosi, P.; Berveiller, M.; Zaoui, A. Latent hardening in copper and aluminium single crystals. *Acta Metallurgica* **1980**, *28*, 273–283.
34. abd J. L. Bassani, T.Y.W.; Laird, C. Latent hardening in single crystals - I. Theory and experiments. *Proceedings of the Royal Society of London A: Mathematical, Physical and Engineering Sciences* **1991**, *435*, 1–19.
35. Marchenko, A.; Mazière, M.; Forest, S.; Strudel, J.L. Crystal plasticity simulation of strain aging phenomena in α-titanium at room temperature. *International Journal of Plasticity* **2016**, *85*, 1–33.
36. Tabourot, L.; Fivel, M.; Rauch, E. Generalised constitutive laws for f.c.c. single crystals. *Materials Science and Engineering: A* **1997**, *234-236*, 639–642.
37. Héripré, E.; Dexet, M.; Crépin, J.; Gélébart, L.; Roos, A.; Bornert, M.; Caldemaison, D. Coupling between experimental measurements and polycrystal finite element calculations for micromechanical study of metallic materials. *International Journal of Plasticity* **2007**, *23*, 1512–1539.
38. Shi, Q.; Latourte, F.; Hild, F.; Roux, S. Backtracking Depth-Resolved Microstructures for Crystal Plasticity Identification—Part 2: Identification. *JOM* **2017**, *69*, 2803–2809.
39. Barabash, R.I.; Klimanek, P. X-ray scattering by crystals with local lattice rotation fields. *Journal of Applied Crystallography*, *32*, 1050–1059.
40. Pantleon, W.; Wejdemann, C.; Jakobsen, B.; Lienert, U.; Poulsen, H. Evolution of deformation structures under varying loading conditions followed in situ by high angular resolution 3DXRD. *Material Science and Engineering A* **2009**, *524*, 55–63. Special Topic Section: Probing strains and Dislocation Gradients with diffraction.
41. Borbély, A.; Ungár, T. X-ray line profiles analysis of plastically deformed metals. *Comptes Rendus Physique* **2012**, *13*, 293–306. Use of large scale facilities for research in metallurgy / Utilisation des grands instruments pour la recherche en métallurgie.